INTERNATIONAL JOURNAL OF HYDROGEN ENERGY 46 (2021) 19599–19616

Available online at www.sciencedirect.com

ScienceDirect

journal homepage: www.elsevier.com/locate/he

Reconstruction model for heat release rate based on artificial neural network

Bo Li [a,b], Wei Yao [a,b,*], Yachao Lee [a,b], XueJun Fan [a,b,**]

[a] Institute of Mechanics (CAS), Key Laboratory of High-Temperature Gas Dynamics, Institute of Mechanics, CAS, Beijing 100190, China

[b] Institute of Mechanics (CAS), School of Engineering Science, University of Chinese Academy of Science, Beijing 100049, China

HIGHLIGHTS

- An efficient yet accurate reconstruction model for heat release rate (HRR).
- Reconstruction model based on reduced-order POD method and data-driven ANN model.
- Validation of the HRR reconstruction model in a supersonic hydrogen flame.
- Accurate HRR reconstruction from measurable chemiluminescent species.
- Generalization of current framework to hydrocarbon combustion is feasible.

ARTICLE INFO

Article history:
Received 16 August 2020
Received in revised form
3 March 2021
Accepted 9 March 2021
Available online 12 April 2021

Keywords:
Heat release rate (HRR)
Artificial neural network (ANN)
Proper orthogonal decomposition (POD)
Chemiluminescence
Supersonic hydrogen flame

ABSTRACT

Optimizing the distribution of heat release rate (HRR) is the key to improve the performance of various combustors. However, limited by current diagnostic techniques, the spatial measurement of HRR in many realistic combustion devices is often difficult or even impossible. HRR prediction is theoretically possible through establishing correlations between HRR and other quantities (e.g., chemiluminescence intensity) that can be experimentally determined; however, up to now, few universal correlations have been established. A novel artificial neural network (ANN) approach was adopted to build the mapping relationship between the combustion heat release rate and the measurable chemiluminescent species. Proper orthogonal decomposition (POD) technology is used to extract the combustion physics and reduce the data of the spatial-temporally high-resolution combustion field. The correlation between the reduced-order HRR and chemiluminescent species is built using an ANN model. A unique segmentation approach was proposed to improve the training efficiency and accuracy. Validation in a supersonic hydrogen-oxygen nonpremixed flame proves the accuracy and efficiency of the proposed HRR reconstruction model based on the reduced-order POD method and data-driven ANN model.

© 2021 Hydrogen Energy Publications LLC. Published by Elsevier Ltd. All rights reserved.

* *Corresponding author*. Institute of Mechanics (CAS), Key Laboratory of High-Temperature Gas Dynamics, Institute of Mechanics, CAS, Beijing 100190, China.

** *Corresponding author*. Institute of Mechanics (CAS), Key Laboratory of High-Temperature Gas Dynamics, Institute of Mechanics, CAS, Beijing 100190, China.

E-mail addresses: libo2@imech.ac.cn (B. Li), weiyao@imech.ac.cn (W. Yao), liyachao@imech.ac.cn (Y. Lee), xfan@imech.ac.cn (X. Fan).

https://doi.org/10.1016/j.ijhydene.2021.03.074

0360-3199/© 2021 Hydrogen Energy Publications LLC. Published by Elsevier Ltd. All rights reserved.

Nomenclatures

p	pressure, Pa
T	temperature, K
ρ	density, $kg \cdot m^{-3}$
u	velocity, m/s
R_u	universal gas constant
ν_t	eddy viscosity
τ_{ij}	viscous stress tensor
i	time index during navigation
j	waypoint index
Pr_t	turbulent Prandtl number
Sc_t	turbulent Schmidt number
$\tilde{Y}_k$	mass fraction of species k
$\overline{\omega}_k$	time-averaged mass production rate of species k
MSE	the mean squared error
HRR	Heat release rate
ANN	Artificial Neural Network
POD	Proper Orthogonal Decomposition
LES	large-eddy simulations

Introduction

Heat release rate (HRR) is a key index in characterizing the combustion system. It is significant for the understanding and prediction of unsteady flame behaviors such as combustion noise, combustion thermoacoustic instability, and pulsed combustion [1–3]. For practical combustors, when combustion instabilities are initiated by flow unsteadiness interacting with heat-release fluctuations, severe structural damage can be resulted in. For scramjets, optimizing the distribution of heat release rate was necessary to control combustion modes, improve combustion efficiency and increase thrust [4]. On the other hand, the heat release rate from an unwanted fire is a major indication of the threat of the fire to life and property. Therefore, the development of accurate predictive tools for HRR distribution in flames is expected to be beneficial for the development of combustion monitoring and control techniques [5].

However, HRR is more like a theoretical variable [2] since the spatial measurement of HRR in many combustion devices is often impractical [6]. There is no existing method that can real-time diagnose the spatial distribution of HRR emitted from combustion. Among both intrusive and non-intrusive instruments, only the cone calorimeter can measure a total heat release in terms of oxygen consumption. The developing non-intrusive chemiluminescence [7] measurement technology is one effective diagnostic methodology to obtain the species distribution with both high spatial and temporal resolutions. This provides a promising approach to obtain HRR distribution reversely from the distribution of chemiluminescent species. Hardalupas et al. [8] studied the relationship between radiation intensity and tensile strength and equivalence ratio using the Cassegrain teleseismic imaging system in a collision-premix natural gas flame. Their results show that the peak intensity of OH*, CH*, and C2* can mark the maximum heat release rate well, but the quantitative relationship between radiation intensity and heat release rate was not given. Panoutsos and Taylor et al. [9] analyzed various calculation models of OH* and CH*s and showed that the intensity of OH* and CH* can qualitatively reflect the HRR, but the quantitative relationship between them will change slightly with the equivalence ratio. Both experimental [10–12] and numerical [3,11,13–17] studies pointed out that the integral emissions approximate the spatial distribution of HRR is more practical [2,18–21], while such inversion method is, on the other hand, very complicated and can only provide qualitative analysis for the HRR. Quantitative diagnosis is usually of practical significance. However, due to the intrinsic complexity of combustion physics, no quantitative relationship between chemiluminescent intensity and HRR has been obtained in previous studies. This study focuses on developing a quantitative mapping relationship between HRR and chemiluminescent species, with the purpose of conveniently deriving HRR distribution in a real combustion scenario.

Artificial Neural Network (ANN) [22], as a promising machine-learning and artificial intelligence methodology, has shown its powerful ability to simulate the underlying mechanisms of complex data sets, so it can be trained to correlate the HRR with selected chemiluminescent species. A typical multilayer ANN architecture consists of three main parts: an input layer, hidden layers, and an output layer. The number of hidden layers determines the "depth" of the model [23]. ANN provides a modular and agile modeling framework that can be tailored to address many challenges in fluid mechanics [24–29]. ANN was not only used to resolve the ordinary and partial differential equations [30–32] in dynamical systems and fluid mechanics but also was applied in heat transfer [33], turbulent flows [34], and many other aeronautic problems [35]. More recently, ANN applications have been made to function approximation, turbulence and turbulent combustion closure, flow control, data association, and optimization [36–39]. Xiao et al. [40], Ling et al. [28], Wang et al. [41], and Singh et al. [42] have employed ANN models to identify and model the anisotropic turbulence. Maulik et al. [43] have successfully predicted the turbulence source terms in large eddy simulation (LES) using coarsely resolved quantities using a multi-layered ANN model. Lapeyre et al. [25] have employed a convolutional neural network (CNN) to emulate the subgrid-scale (SGS) flame surface density in LES. Ihme [27], Shadram et al. [44], Owoyele et al. [24], and Bhalla et al. [45] applied ANN to approximate nonlinear functions with high-dimensional data and replace the memory-intensive tabulation method by memory-efficient ANN models.

The raw data of HRR and chemiluminescent species pose high costs and low convergence for ANN training. Instead, reduced-order models (ROMs) can be employed. Proper orthogonal decomposition (POD) is a sophisticated reduced-order technique and has been applied in many different fields: data compression, image processing, dynamical systems, and fluid mechanics [46–50]. The coupling between POD and machine learning models has been succesfully employed for the emulation and extraction of physics [47,51–56].

Aiming to develop an ANN-POD coupled reconstruction model to correlate HRR with chemiluminescent species, the paper is structured as follows. Section Introduction puts

forward the current research status in HRR diagnosis, POD, and ANN. Section Framework for HRR reconstruction introduces the physical models, numerical methods, and reconstruction framework. In the reconstruction framework, POD technology is used to extract the combustion physics and reduce the data of the spatial-temporally high-resolution combustion field, then the correlation between the reduced-order HRR and chemiluminescent species is built using an ANN model. Section Results and discussion presents the realization of HRR reconstruction from OH in a demo case, where the reconstruction framework of HRR is verified by a high-resolution LES modeling of a supersonic oxyhydrogen non-premixed flame of Evans's experiment, and the chemiluminescent species of OH is selected as the input of chemiluminescent species because it has been proved to be a good marker of the main heat release rate region [57–59]. The conclusions in Section Conclusion elaborate on the prospects of the proposed HRR reconstruction model.

Framework for HRR reconstruction

Artificial neural network

Backpropagation Artificial Neural Network (BP-ANN) is trained to build the connection between HRR and chemiluminescent species. A similar implementation has been realized in Li et al. [60], and a brief review of the methodology is given below.

As shown in Fig. 1, a typical multilayer BP-ANN architecture usually consists of three main parts: an input layer, some hidden layers, and an output layer. Each layer is composed of individual neurons operating in parallel. The input layer is used to load the known parameters X, e.g., the chemiluminescent species in this study. The hidden layer is set to accommodate all the known information and build a nonlinear relationship between the input parameters and the output results. The output layer is utilized to resolve the unknown results Y from the hidden layer, e.g., HRR in this study. Once the number of hidden layers and the number of neurons in each hidden layer were determined, the connection weights between the neurons were adjusted by information transmitting forward and errors transferring backward during training. Any errors made by the network during training were fed back sent to correct the neuron weights and teach the network what is right and wrong, as schematically illustrated in Fig. 1. During the learning process, the error is estimated by the mean squared error (MSE) defined as,

$$MSE = \frac{1}{n}\sum_{i=1}^{n}(y_i - t_i)^2 \tag{1}$$

where y_i , n is the network output value and the total number respectively, t_i is the target value. Smaller MSE values indicate better ANN performance. When the MSE reaches a minimum, or the steps of training reach the predefined maximum steps, the network training is terminated, and the weights are stored.

Fig. 2 illustrates how signals are processed through a single neuron. First, the neuron receives weighted activations from other neurons and added up. The summation is then passed through an activation function f, the outcome α is transferred to the next layer's neurons as a new activation. Activation functions determine the output of a deep learning model through a series of nonlinear transformations on the input, making the trained model capable of learning and performing more complex tasks. During the backpropagation, the gradients are supplied along with the errors to update the weights and biases, so the activation functions should be differentiable and monotonic. Recently, the nonlinear activation functions such as logistic sigmoid, hyperbolic tangent (tanh), and rectified linear unit (ReLU) are popular activation functions in deep learning, while the sigmoid function is the most frequently used activation function in recent studies. Both sigmoid and tanh have S-Shaped curves; the only difference is that sigmoid lies between 0 and 1 while tanh lies between 1 and -1. The wide-spanning range of tanh function makes the model based on it learns more slowly. ReLU function can greatly accelerate the convergence of stochastic gradient descent compared with sigmoid and tanh activation functions. However, it may encounter the problem of dying neurons, which stop responding to the variations of the output error. In comparison, sigmoid function is differentiable across its entire domain, efficient to compute with, and can lead to a faster convergence rate. This study adopts the logistic sigmoid activation function given by:

$$f(z) = \frac{1}{1 + e^{-z_n}} \tag{2}$$

where $z_n = \sum_{j=1}^{n} x_j W_{ij}$ is the weighted sum of the input activations for each neuron.

During the backpropagation, the weights were updated according to the gradient descent algorithm [61,62]. The change of weight W_{ij} in the connection neuron from i to j is written as:

$$\Delta W_{ij} = -l_r \frac{\partial MSE}{\partial W_{ij}} \tag{3}$$

Here an appropriate learning rate l_r plays an important role in the training, since the abrupt change caused by a large l_r may miss the minimum while the low learning rate caused by a small l_r slows down the training. In order to minimize the error function MSE, W_{ij} needs to be decreased when $\frac{\partial MSE}{\partial W_{ij}} > 0$, and increased when $\frac{\partial MSE}{\partial W_{ij}} < 0$. In order to avoid oscillation inside the network such as alternating connection weights, and to improve the convergence rate, an adaptive learning rate was adopted [63]. Similar to a ball rolling down a mountain, the current rolling speed is determined not only by the local slope of the mountain but also by its own inertia (momentum). Similarly, the change of weight W_{ij} at time (t+1) is $\Delta W_{ij}(t+1)$, written as

$$\Delta W_{ij}(t+1) = (m-1) l_r \frac{\partial MSE}{\partial W_{ij}} + m \Delta W_{ij}(t) \tag{4}$$

where m is the momentum varying in the range of [0, 1].

To avoid overfitting and make sure that the final trained model performs well not just on the training data but also on new inputs, a regularization strategy of early stopping was adopted in this study. Early stopping is an unobtrusive form of regularization because it requires nearly no change

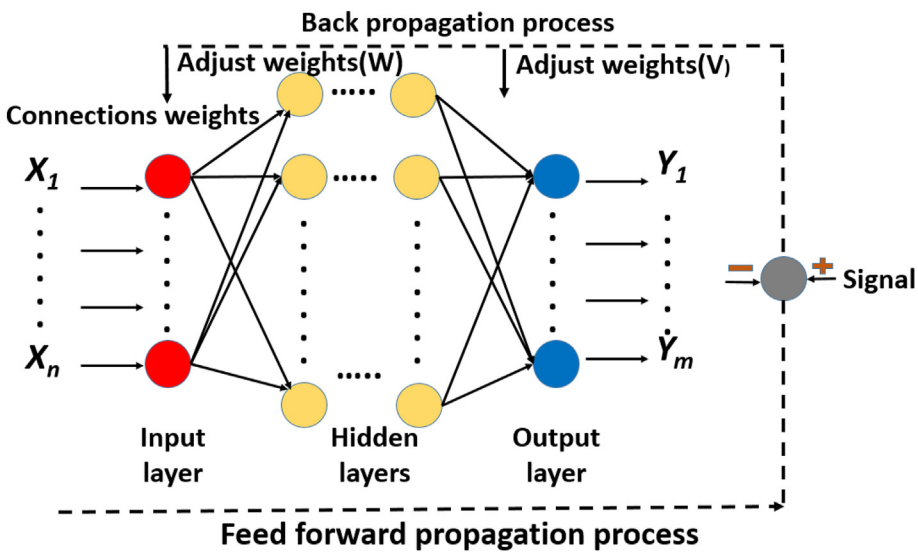

Fig. 1 – Schematics of the three-layer BP-ANN.

in the underlying training procedure, the objective function, and the set of allowable parameter values. It is also the reason why the MSE equation (Eq. (28)) does not contain an explicit regularization term. The early stopping strategy works by monitoring the validation set error to terminate the trajectory at a point with the lowest validation set error. In this view, the number of training steps is just another hyperparameter. Usually, when the training epochs reach a certain number, the validation set error (ValidationSetMSE) will reach a small value and drops negligibly later. Momentum is not only a technique to keep the weight changing in the direction of the previous step to speed up the convergence but also has the benefit of avoiding the abrupt change in the opposite direction once the direction reverses. To avoid an excessive influence of the momentum on the weight update, a momentum adaptation technique was also developed in combination with the learning rate adaptation [64].

Proper orthogonal decomposition

Proper Orthogonal Decomposition (POD) is a mathematical procedure for extracting a basis of a modal decomposition from an ensemble of signals, which was first introduced in the context of fluid mechanics by Lumley [65]. The most attractiveness of the POD lies in the fact that it is a linear procedure, and this kind of mathematical property makes it

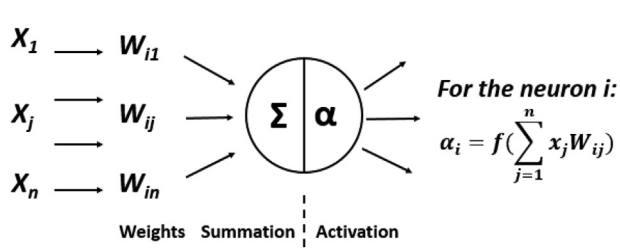

Fig. 2 – Information processing in a single neural-network neuron.

a preferred basis to use in many nonlinear circumstances. In this section, a brief discussion of the main features of POD will be given below, and further details on the mathematical formulation can be found in the following references.

In this study, the vector of flow quantities $q(x,t)$, which is assumed to be a function of space and time, is decomposed as the sum of the time-averaged flow $\overline{q}(x)$ and the fluctuation $q'(x,t)$,

$$q(x,t) = \overline{q}(x) + q'(x,t) \tag{5}$$

The so-called "snapshot POD" technique [66] is used to address the fluctuating combustion fields. In the snapshot POD analysis, the mean field of all snapshots in a series is calculated and then subtracted from the snapshots to give the fluctuating part of the snapshots, which was arranged in a matrix q'. Assuming that sampling time is N and the number of data points is M, each snapshot is formulated as a column in the matrix, which has a total of N columns and M rows. q' is expressed as

$$q' = [q'^1\ q'^2 \ldots q'^N] = \begin{bmatrix} q'^1_1 & q'^2_1 & \cdots & q'^N_1 \\ q'^1_2 & q'^2_2 & \cdots & q'^N_2 \\ \vdots & \vdots & \vdots & \vdots \\ q'^1_M & q'^2_M & \cdots & q'^N_M \end{bmatrix} \tag{6}$$

The vector of primitive variables can be generalized as $q' = (\dot{Q}, Y_{OH})_t$, where $\dot{Q}$is the heat release rate, Y_{OH} is the mass fraction of OH. In POD, the fluctuation quantities, $\acute{q}(x,t)$, can be expanded as the combination of POD modes $\varnothing_i(x)$ in M-vector form and their temporal model coefficients $a_i(t)$ for a given mode number of N,

$$q'(x,t) = \sum_{i=1}^{N} a_i(t)\varnothing_i(x) \tag{7}$$

In order to compute $\varphi_i(x)$ and $a_i(t)$, the covariance matrix **C** is defined to describe the temporal correlation of the flow field,

$$\mathbf{C} = \frac{1}{N} q'^T q' = \frac{1}{N} \left(q'(x, t_i), q'(x, t_j) \right)_\Omega \tag{8}$$

Then, the eigenvalues λ and eigenvectors A are obtained from:

$$\mathbf{CA} = \lambda \mathbf{A} \tag{9}$$

where the eigenvalues λ_i are sorted in descending order, and the eigenvectors are sorted in the same order, as shown in Eq. (10). The magnitude of the n-th eigenvalues depicts the energy contribution of the n-th eigenmode. When the total energy of the fluctuating field is obtained by the sum of the eigenvalues as in Eq. (11), the relative energy ratio of the i-th eigenmode is calculated as in Eq. (12).

$$\lambda_1 > \lambda_2 > \ldots > \lambda_N = 0 \tag{10}$$

$$E = \sum_{i=1}^{N} \lambda_i \tag{11}$$

$$k_i = \lambda_i / E \tag{12}$$

The spatial eigenfunctions $\varnothing_i(x)$ of the POD modes is defined as:

$$\varnothing_i(x) = \frac{\sum_j^N A_i q'^j}{\left\| \sum_j^N A_i q'^j \right\|}, \; j = 1 \ldots N \tag{13}$$

where A_i is the i-th eigenvector corresponding to λ_i from Eq. (11), q'^j is the j-th component of the snapshot matrix $\boldsymbol{q}'$ in Eq. (6). As the flow field is decomposed, the spatial eigenfunctions are only dependent on the position, and the temporal mode amplitudes are only functions of time. The temporal mode coefficients for the j-th snapshot can then be computed as,

$$a_i(t) = \varnothing_i q'^j (x, t_j) \tag{14}$$

When the number of modes N_{pod} is equal to the number of snapshots N, the original flow field can be perfectly reconstructed as in Eq. (7). Otherwise, if $N_{pod} < N$, the flow reconstruction is an approximation to the original field. However, in most cases, the first few modes take the vast majority of the total energy, suggesting that they are associated with the dominant energetic flow structures. This gives the convenience of reducing the order of the time-variant flow field to a limited number of POD modes.

HRR reconstruction

Fig. 3 schematically shows the overall framework of the HRR reconstruction method comprising pre-processing, POD extracting, ANN training, and final reconstruction. The workflow is: 1) firstly extracting the main POD base modes to significantly compress the field data of OH and HRR generated by LES, 2) then establishing the correlation between the POD mode coefficients of OH and HRR by the ANN model, 3) finally reconstructing the HRR distribution from a new data set of chemiluminescent species based on the POD coefficients predicted by the trained ANN model and the POD base modes.

Considering that the experimental data are usually scarce and temporally inconsistent, experimentally validated high-fidelity LES data are used to validate the proposed ANN-POD reconstruction method. Defining the flow-through time (FTT) as the stream washing out the computational domain, a total of 3000 snapshots were sampled within 2 FTT. To reduce the data volume, snapshots were sampled in the central combustion region of 300 mm × 24 mm. By POD, basis modes and modal coefficients of OH and HRR are extracted. A three-hidden-layer BP-ANN model is used to correlate the modal coefficients of OH and HRR:

$$\mathbf{Y} = \varnothing(\mathbf{X}) \tag{15}$$

where $\varnothing$ is the mapping function, $\mathbf{X}$ is the input vector of modal coefficients for OH, $\mathbf{Y}$ is the output vector of modal coefficients for HRR (termed by dQ).

A unique segmented training approach is developed in this study, as shown in Fig. 4. Since the POD modes are independent of each other, a mapping between all the modal coefficients of HRR with all the modal coefficients of OH can be established, i.e., an m-to-n ANN model with m modal coefficients of OH to n modal coefficients of HRR. Theoretically, one needs to build such a m-to-n ANN model between all the POD modal coefficients of OH and HRR. Considering that the first few POD modes are associated with the most energetic flow structures, as indicated by their large relative energy ratios, the number of ANN models can be significantly reduced. Even so, it is still time-consuming and computationally-expansive to conduct the ANN training of m-to-n. By segmenting the total n output data sets into l subsets, each segmentation subset consists of n/l modal coefficients. Then individual ANN models of m-to-n/l for each segmentation data will be separately trained. The training is conducted by a cross-validation approach, which divides the training data set into several divisions after randomly disrupting the data order, and uses one as the validation set while the other nine as the training set.

After the successful training of the ANN models, the modal coefficients of HRR can be derived from the modal coefficients of OH, and then the HRR fields can be reconstructed based on the derived modal coefficients and the previously-obtained POD modes.

Validation case: Evans' supersonic hydrogen flame

Fig. 5 shows a schematic of a simplex shear-coaxial injector representative of those commonly used in hydrogen-fueled rocket engines. The experiment was conducted by Evans et al. [67]. As shown in Fig. 5, supersonic hydrogen is injected through a circular nozzle at a Mach number of 2 and 251 K, to the center of vitiated air, which is at nearly the same Mach number of 1.9 but with a higher temperature of 1495 K. Before mixing, the airflow will be preheated by burning with hydrogen and then replenished with oxygen to maintain an

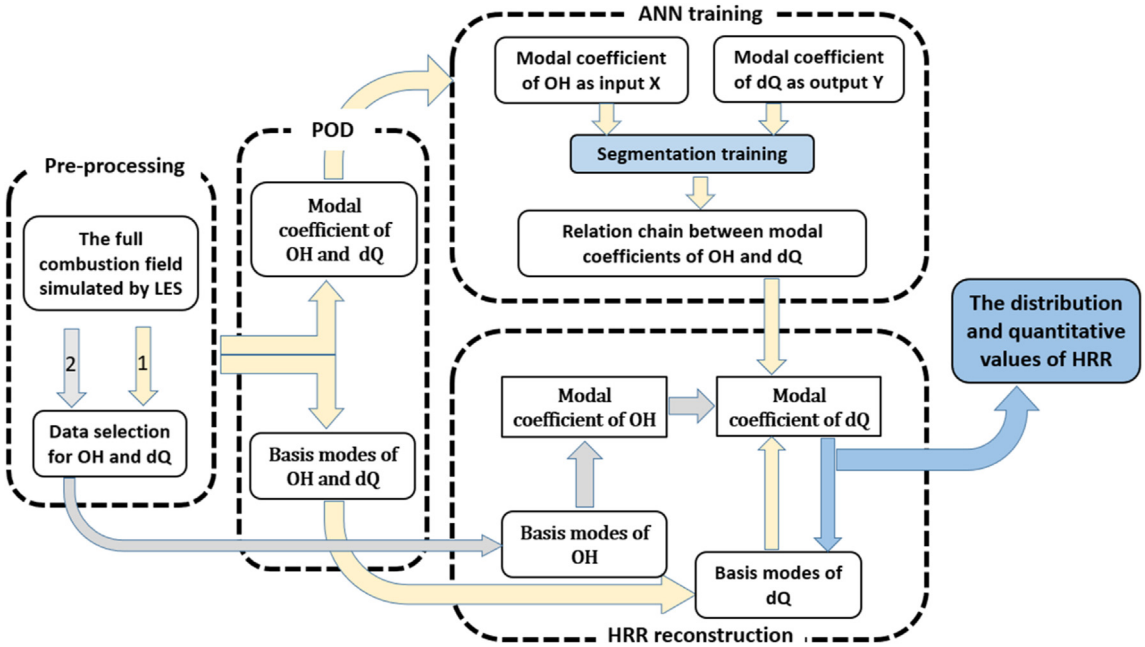

Fig. 3 – The framework of HRR reconstruction comprising pre-processing, POD extracting, ANN training, and reconstruction.

oxygen volume fraction equal to the ambient condition. In the following, spatial coordinates are scaled with the outer diameter of the hydrogen tube, $D = 9.525$ mm, including the inner diameter of 6.525 mm and the wall thickness of 1.5 mm. Table 1 provides the boundary conditions of the experiment. The mass fractions of stable species, i.e., N_2, O_2, H_2, and H_2O were measured in the Evans' experiment by conventional probe technique at four axial planes of $x/D = 8.26$, 15.5, 21.7, and 27.9. Though intermediate radical species were not available, the abundant measurement data can be used to calibrate an LES modeling.

Numerical details of the validation case

A. Governing equations

In this study, the numerical modeling was conducted by Large Eddy Simulation (LES), in which large-scale turbulent structures are directly resolved while small dissipative structures are modeled. LES solves the unsteady three-dimensional Favre-averaged spatially-filtered compressible Navier-Stokes (N–S) equations of mass, momentum, energy, and species concentration,

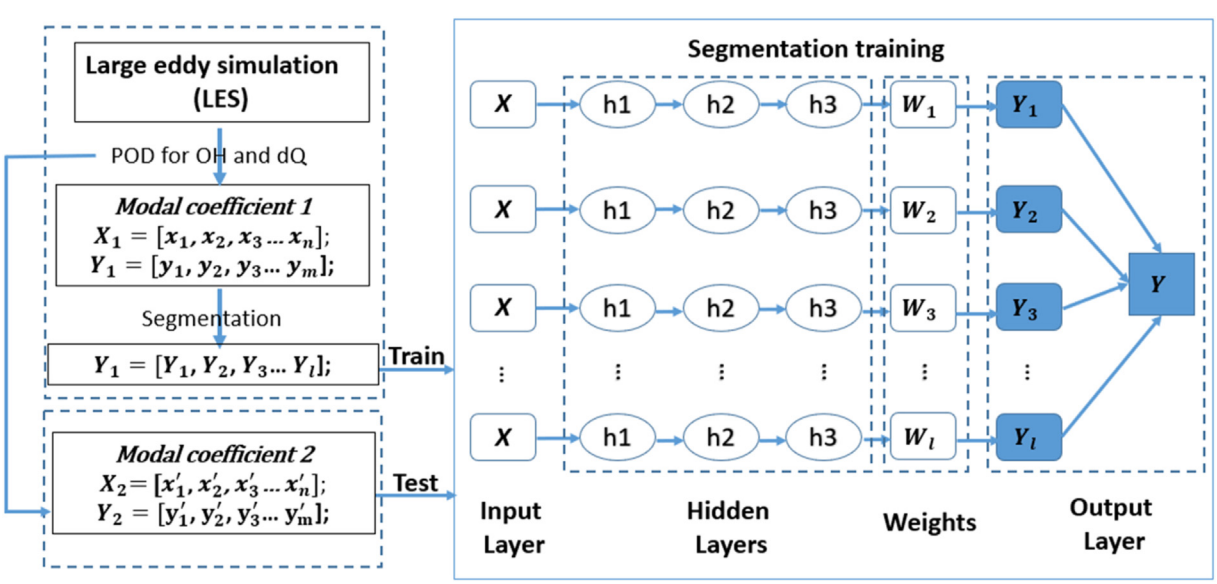

Fig. 4 – Schematic diagram of the segmentation training process conducted by three-hidden layers ANN.

$$\frac{\partial \overline{\rho}}{\partial t}+\frac{\partial \overline{\rho}\tilde{u}_j}{\partial x_j}=0 \tag{16}$$

$$\frac{\partial \overline{\rho}\tilde{u}_i}{\partial t}+\frac{\partial \overline{\rho}\tilde{u}_j\tilde{u}_i}{\partial x_j}+\frac{\partial \overline{p}}{\partial x_i}-\frac{\partial \tilde{\tau}_{ij}}{\partial x_j}=-\frac{\partial \tau_{ij}}{\partial x_j} \tag{17}$$

$$\frac{\partial \overline{\rho}\tilde{H}_t}{\partial t}+\frac{\partial \overline{\rho}\tilde{u}_j\tilde{H}_t}{\partial x_j}-\frac{\partial}{\partial x_j}\left(\overline{\rho}D_T\frac{\partial \tilde{H}_t}{\partial x_j}+\sum_{k=1}^{L}\overline{\rho}D_k\frac{\partial \tilde{Y}_k}{\partial x_j}\tilde{H}_k\right)-\frac{\partial \overline{p}}{\partial t}-\frac{\partial \tilde{u}_j\tilde{\tau}_{ij}}{\partial x_j}=-\frac{\partial \Psi_{T,j}}{\partial x_j} \tag{18}$$

$$\frac{\partial \overline{\rho}\tilde{Y}_k}{\partial t}+\frac{\partial \overline{\rho}\tilde{u}_j\tilde{Y}_k}{\partial x_j}-\frac{\partial}{\partial x_j}\left(\overline{\rho}D_k\frac{\partial \tilde{Y}_k}{\partial x_j}\right)=-\frac{\partial \Psi_{k,j}}{\partial x_j}+\overline{\omega}_k \tag{19}$$

$$\overline{p}=\overline{\rho}R\tilde{T} \tag{20}$$

where the over bar "-" and the tilde "~" represent spatial-filtering variables and Favre-filtering operation respectively, t denotes the time; The variables p , T, ρ, τ_{ij} , u_i is the pressure, temperature, density, viscous stress tensor and the velocity in x_i direction (spatial dimension $i = 1, 2, 3$), respectively; $\tilde{H}_t = \tilde{H} + 0.5\tilde{u}_i^2$ is the total absolute enthalpy obtained as the sum of the absolute enthalpy $\tilde{H}$ and the resolved kinetic energy; $\tilde{Y}_k$ and $\overline{\omega}_k$ represents the mass fraction and the averaged mass production rate of species k ($k = 1, \ldots, L$, with L the total species number), respectively; D_k and D_T denotes the mixture-averaged mass diffusivity and the thermal diffusivity, respectively. For the combustion is considered far from the drastic phase-change region, the ideal gas law is employed to relate the density, temperature and pressure of the gas, in which $R = R_u/W$ is the gas constant of gas mixture and R_u is the universal gas constant, W is the molar weight of the multicomponent mixture and defined by:

$$W=\left(\sum_{k=1}^{L}Y_k/W_k\right)^{-1} \tag{21}$$

The Soret and Dufour effects are neglected in the present study because of its small contribution in Eqs. (3) and (4).

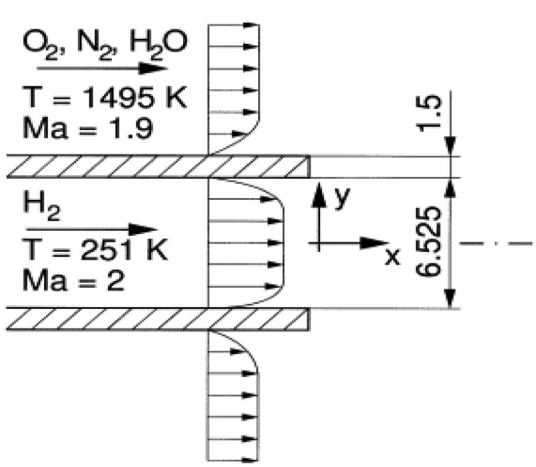

Fig. 5 – Schematics of the supersonic diffusion flame experiment by Evans et al.

Table 1 – Experimental boundary condition.

	Hydrogen	Vitiated air
Mach number	2	1.9
Velocity	2432 m/s	1510 m/s
Static temperature	251 K	1495 K
Static pressure	1 bar	1 bar
Composition		
Y_{H_2}	1	0
Y_{O_2}	0	0.241
Y_{N_2}	0	0.478
Y_{H_2O}	0	0.281

According to the Stokes's hypothesis, the computable average momentum diffusive flux for a Newtonian fluid is given by:

$$\tilde{\tau}_{ij}=\overline{\rho}\nu\left(\tilde{T}\right)\left(2\tilde{S}_{ij}-\frac{2}{3}\delta_{ij}\tilde{S}_{kk}\right) \tag{22}$$

where ν is the kinetic viscosity, and $\tilde{S}_{ij}$ is the rate-of-strain tensor of the computable scales,

$$\tilde{S}_{ij}=\frac{1}{2}\left(\frac{\partial \tilde{u}_i}{\partial x_j}+\frac{\partial \tilde{u}_j}{\partial x_i}\right) \tag{23}$$

For the unclosed terms in the N–S equations, additional specific modeling is required. By the gradient diffusion assumption, the turbulent enthalpy flux term $\Psi_{T,j}=\overline{\rho}(\widetilde{u_jH_t}-\tilde{u}_j\tilde{H}_t)$ and the turbulent species diffusion term $\Psi_{k,j}=\overline{\rho}(\widetilde{u_jY_k}-\tilde{u}_j\tilde{Y}_k)$ is modeled as Eq. (9) and Eq. (10), respectively.

$$\Psi_{T,j}=-2\overline{\rho}\frac{\nu_t}{Pr_t}\frac{\partial \tilde{H}_t}{\partial x_j} \tag{24}$$

$$\Psi_{k,j}=-2\overline{\rho}\frac{\nu_t}{Sc_t}\frac{\partial \tilde{Y}_k}{\partial x_j} \tag{25}$$

where ν_t is the eddy viscosity, Pr_t is the turbulent Prandtl number and Sc_t is the turbulent Schmidt number. Both Pr_t and Sc_t are set to unity. The thermodynamic and transport properties of the mixture are calculated by the gas-phase property and chemical kinetics package CHEMKIN-II [68]. Thermodynamic properties are obtained from the NIST-JANAF thermophysical database [69]. Transport properties of the gas mixture, such as viscosity, thermal, and mass diffusivities are calculated based on a CHEMKIN-format transport database [70]. The mixture thermal diffusivity is calculated based on the conductivity and specific heat. Viscosity and thermal conductivity are averaged by the modified Wilke's law [71] and the combination averaging, respectively. Mixture-averaged mass diffusivities are used with the mass conservation achieved by setting nitrogen as the inert gas.

The LES simulation will be conducted by a compressible reacting flow solver Amber (formerly known as AstroFoam) [72], which is developed based on the original density-based rhoCentralFOAM solver distributed with the open-source CFD package OpenFOAM [73]. Amber has been successfully applied in a wide range of supersonic flow and combustion modelings [74–77].

B. Turbulence model and turbulent combustion model

The turbulent viscosity is modeled by dynamic subgrid kinetic energy model (DKEM) [78], which has the advantages in modeling the transitional flows and flows with large-scale unsteadiness. The formulation in LES is defined as:

$$\frac{\partial \bar{\rho} k_{sgs}}{\partial t} + \frac{\partial \bar{\rho} \tilde{u}_j k_{sgs}}{\partial x_j} = \frac{\partial}{\partial x_j}\left[\bar{\rho}\left(\left(\frac{\nu_t}{Pr_t} + D_m\right)\frac{\partial k_{sgs}}{\partial x_j}\right)\right] - \tau_{ij}\frac{\partial \tilde{u}_i}{\partial x_j} - C_\varepsilon \frac{\bar{\rho}\left(k_{sgs}\right)^{3/2}}{\bar{\Delta}} \tag{26}$$

$$\nu_t = C_\upsilon \bar{\Delta}\sqrt{k_{sgs}} \tag{27}$$

where C_ε and C_υ are model constants being dynamically determined [79,80], $\bar{\Delta}$ is the characteristic length of the grid filter, D_m is the laminar diffusivity equals to the viscosity assuming a laminar Pt = 1.

For combustion chemistry, Burke's detailed hydrogen-oxygen chemical mechanism with nine species and 19 reversible reaction steps was adopted [81,82]. Additionally, in the present study, the partially stirred reactor model (PaSR) was employed to account for the turbulence-chemistry interaction. PaSR assumes that each computational cell is divided into two parts: a reacting part and a non-reacting zone, and in the former region, the diffusion and mixing rate of molecules in a single cell is considered infinitely fast. The averaged turbulence-affected chemical reaction rate $\overline{\omega}_k$ is calculated as,

$$\overline{\omega}_k = \omega_k \frac{\tau_c}{\tau_c + \tau_{mix}} \tag{28}$$

where ω_k is the Arrhenius reaction rate integrated over the current time step, τ_c is the characteristic timescale of chemical reactions calculated as the reciprocal of the largest positive eigenvalue of the chemical source term Jacobian matrix; τ_{mix} is the turbulent micromixing timescales, defined as,

$$\tau_{mix} = C_{mix}\sqrt{\frac{(\upsilon_t \cdot \upsilon)^{1/2}}{\varepsilon}} \tag{29}$$

where the constant value of C_{mix} is a set as 1.0, ε is the dissipation rate of turbulent kinetic energy and defined as $\varepsilon = 2\upsilon_{eff}\left|\tilde{S}_{ij}\right|^2$, $\upsilon_{ef} = \upsilon_t + \upsilon$ is the mixture viscosity as the sum of the turbulent viscosity and the mixture dynamic molecular viscosity.

C. Mesh and boundary condition

As shown in Fig. 6, the current modeling was performed on a three-dimensional block-structured hexahedral grid with an axisymmetric pattern. Different from the previous work of Möbus et al. [83], who used axisymmetric two-dimensional mesh to reduce the numerical effort, a full-domain mesh is used in this study to eliminate the influence of symmetry boundary [84]. The computational domain consists of a cylinder of size 300 mm × 40 mm in the flow and radial directions, respectively. The radial

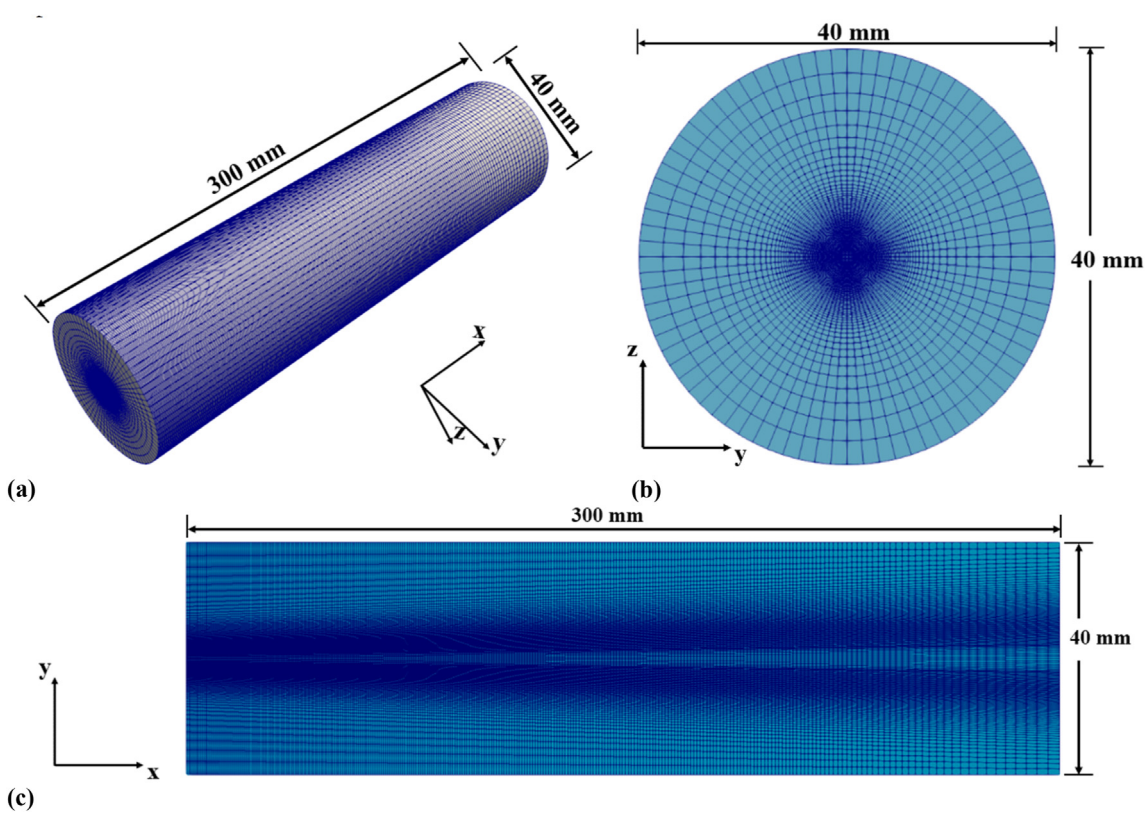

Fig. 6 – Computational grid distribution: (a) global view, (b) top view at x/D = 0, (c) side view at z/D = 0.

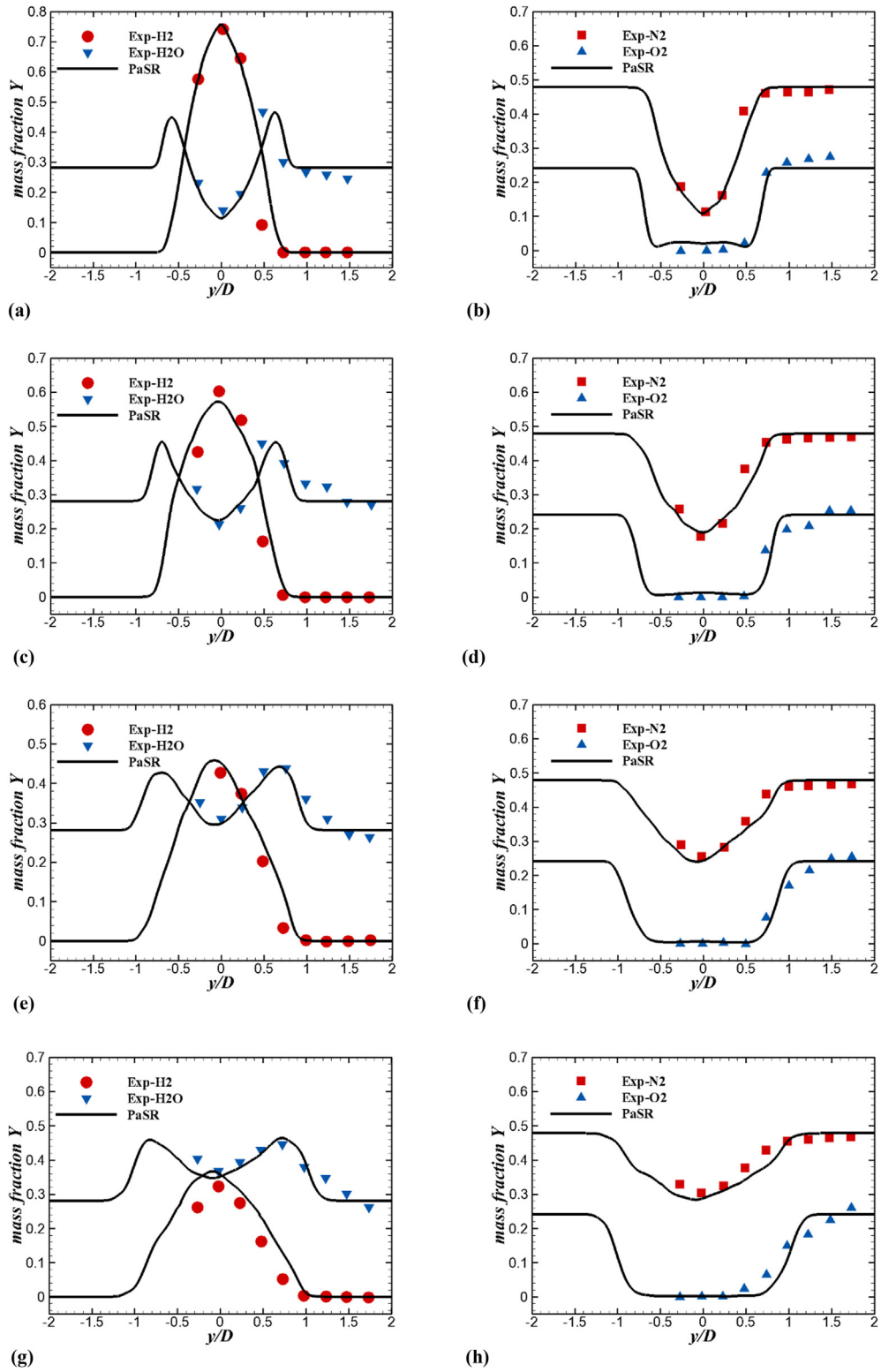

Fig. 7 – The comparison of time-averaged mass fraction distribution at different streamwise locations, (a)–(b) x/D = 8.25, (c)–(d) x/D = 15.5, (e)–(f) x/D = 21.7, (g)–(h) x/D = 27.9.

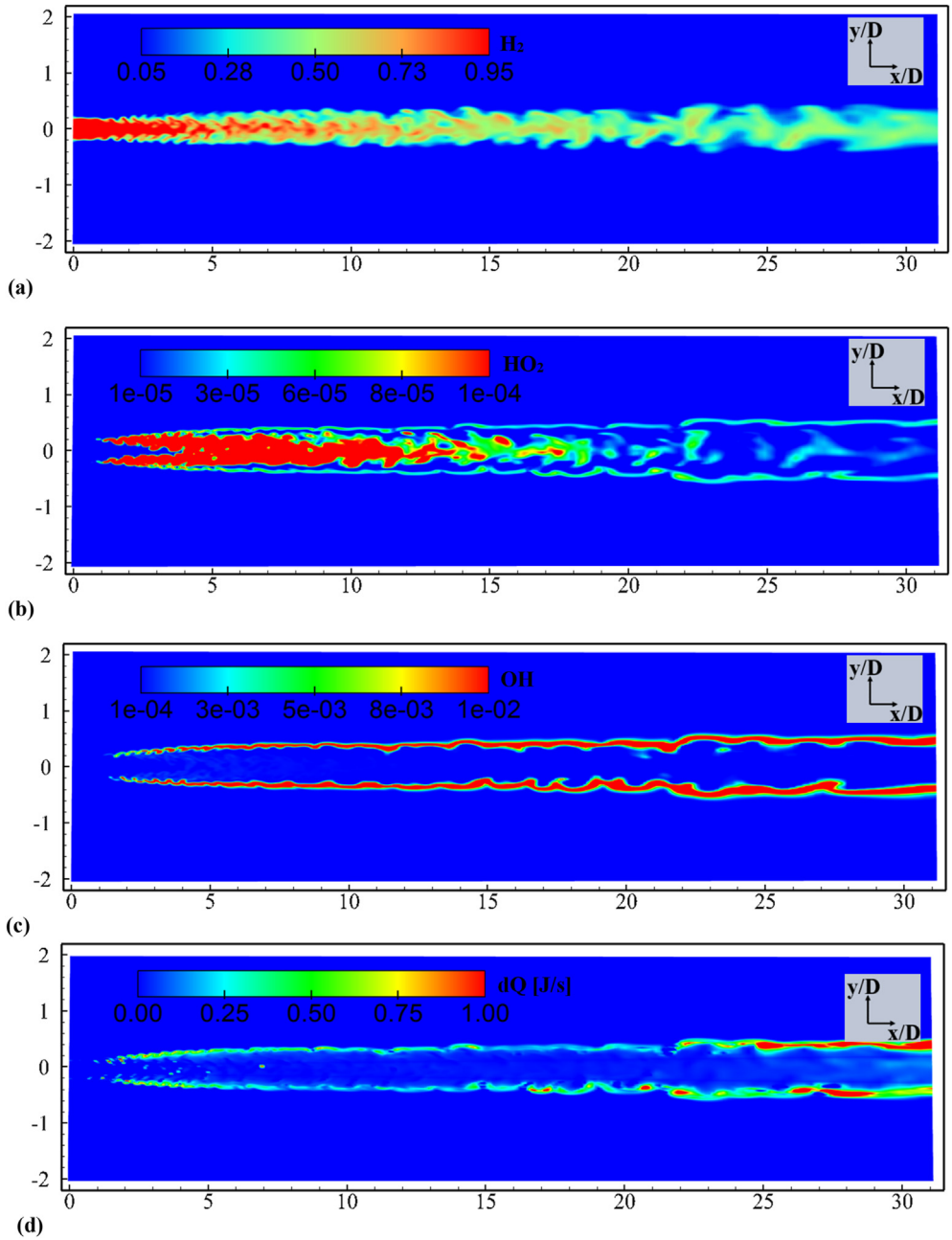

Fig. 8 – Magnitudes of instantaneous (a) H_2, (b) HO_2, (c) OH, and (d) heat release rate on the centerplate for the supersonic diffusion flame.

direction was extended from the hydrogen tube's outer wall for an additional distance of 2*D*, where *D* is the outer diameter of the hydrogen tube, to minimize the restriction of open boundary to flame development. The total grid size is 1.728 million, of which there are 301 points along the flow direction, 85 points in the circumferential direction, and 71 points in the normal direction. To better resolve the shear layer region, the mesh contains a refinement region of high resolution for the jet core and the jet shear layer, as shown in Fig. 2(b) and (c). A relatively coarser grid is generated in the far-field to avoid wave reflections as well as to reduce the computational cost.

Fixed pressure, temperature, and velocity on the oxygen and fuel inlets are set according to those listed in Table 1. The velocity and temperature profiles on the inlets are slightly modified to embody the momentum thickness according to the modified Crocco's correlation,

$$U = U_0(1 - (d_\omega/\delta))^{1/7} \tag{30}$$

$$T = T_0\left(1 + r\frac{\gamma - 1}{2}Ma_0{}^2\left(1 - \left(\frac{U}{U_0}\right)^2\right)\right) \tag{31}$$

where U_0, Ma_0, and T_0 are the free-stream static value of velocity, Mach number, and temperature, respectively; d_ω is the

distance from the wall; δ is the boundary layer thickness, which is set as 1.66 mm and 3.14 mm for the inner and outer channels, respectively; r and γ are constants of 0.7 and 1.4. For the far-field and the outlet boundaries, the zero-gradient condition is applied for the outflow flux, and the ambient conditions are specified for inflow flux. No-slip and adiabatic conditions are used for all the walls.

Results and discussion

Case validation

Quantitative validation of the LES results against the measurements is conducted before the application of the ANN-POD reconstruction method. The comparisons of predicted and measured radial profiles in Fig. 7 show good agreements for the mean mass fraction of main species, i.e., H_2, O_2, N_2, and H_2O at four downstream locations x/D = 8.25, 15.5, 21.7, and 27.9. Note that the measurements are made only for $-0.3 \leq y/D \leq 1.5$. All numerical predictions match well with the measurements, even at the peak and inflection points. Slightly larger discrepancies can be observed around the shear layer ($0.5 \leq |y/D| \leq 1.5$), where larger combustion-induced unsteadiness occurs.

Fig. 8 shows the contours of instantaneous hydrogen, hydroxyl, HO_2, and heat release rate of the modeled supersonic diffusion flame at a quasi-steady time. The numerical simulation well reproduced the shear layer instability and the unsteady evolution. Near the injector exit (x < 1.0*D*), the H_2 stream has not been observably diluted. The formation of HO_2 indicates successful autoignition at a lift-off distance of around 1*D*. The distributions of HO_2, OH, and dQ are compared in Fig. 8(b)–(d). HO_2 mainly distributes inside the jet core and has a lower concentration in the shear layer, where the reactions are more approaching the final product H_2O. This suggests that a rich HO_2 concentration indicates incomplete combustion and lower heat release. By comparing Fig. 8(b) and (c), it can be seen that the profiles of HO_2 and HRR are quite different. The distributions of OH and HRR have high similarity and a positive proportionality, i.e., a higher OH concentration corresponds to a higher HRR.

POD modes analysis

The data set consisting of 3000 snapshots of transient OH and HRR (dQ) fields are sampled within 2 FTTs during a quasi-steady period. The POD analysis extracts a set of 3000 POD modes. Figs. 9 and 10 show the first six and the 300th POD modes for HRR and OH, respectively. It can be seen that the modes of HRR and OH show high similarity in the size and location of key structures, especially for modes 1 and 2. The first POD mode depicts the averaged flame structure, which indicates that combustion mainly occurs near the shear layer and is gradually strengthened downstream. The second and third modes characterize large-size flow structures formed in the shear layer. As the modal order increases, the size of flow patterns in the corresponding POD mode is reduced. When the

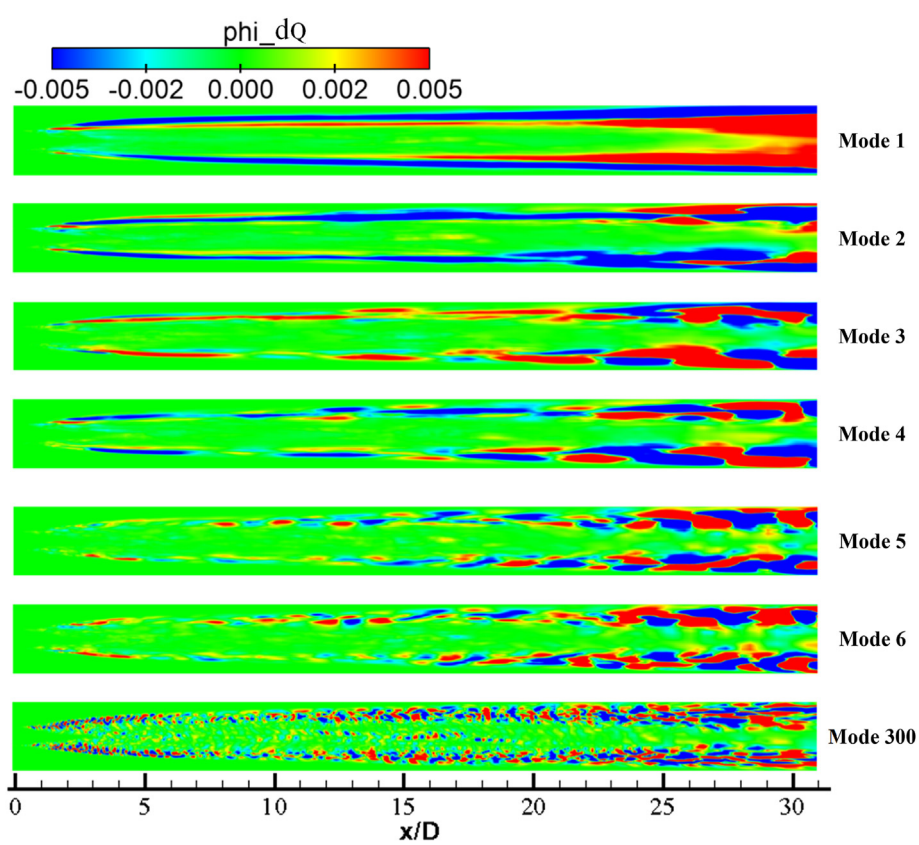

Fig. 9 – The first six and 300th POD modes of HRRs.

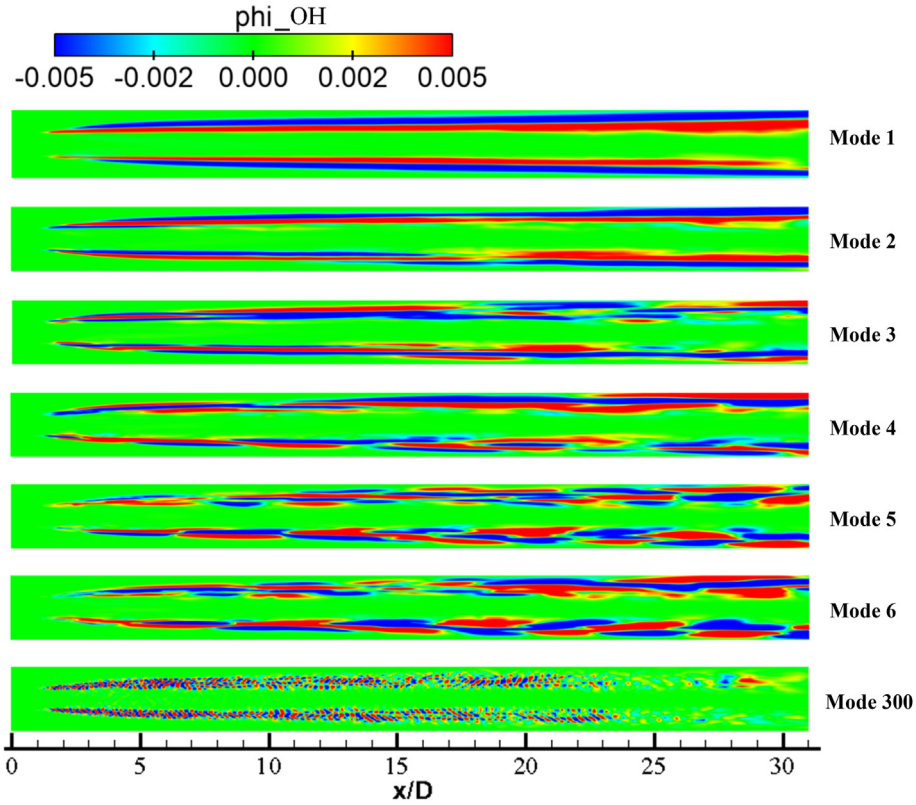

Fig. 10 – The first six and 300th modes of OH.

modal order reaches 300, very fine flow structures are observed. The evolution of transient supersonic flame is composed of complex combinations of all the modes.

Mode selection for ANN training

As aforementioned, using the inputs of the full 3000-mode data poses a high burden for ANN training. To minimize the inputs, the modal energy distribution and the reconstruction proximity by retaining different modal numbers are analyzed. Fig. 11 shows the modal energy distribution for OH and HRR calculated by Eq. (12). The first mode of OH takes 23% of the total energy, while modes 2 and 3 take only 7% and 2.9%. Similarly, for HRR, the first three modes take 7%, 3%, and 2.5% of the total energy. When the modal order reaches 18, the energy ratio drops below 1%. With the further increase of the modal order, the energy ratio approaches zero. The difference between the neighbor modes decreases gradually with the rise of the modal order, and the growth curve becomes almost flattened with the order increasing. The summed energy ratios of the first 50, 100, 210, and 300 modes for HRR are 54.3%, 67.9%, 80.6%, and 85.7%, respectively. For OH, the energy ratio of the first 300 modes is higher than 99%.

Fig. 12 compares the original instantaneous contour of HRR with those reconstructed by using different numbers of POD modes. All the reconstructed approximations capture the main flow patterns, while the accuracy and resolution near the shear layer can be significantly improved by retaining

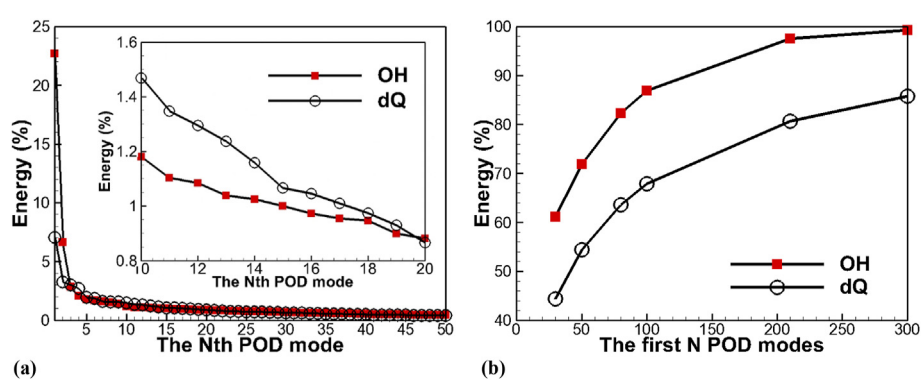

Fig. 11 – The modal energy distribution of OH and HRR, (a) energy ratio for the Nth modal energy, (b) sum of energy ratios for the first N POD modes.

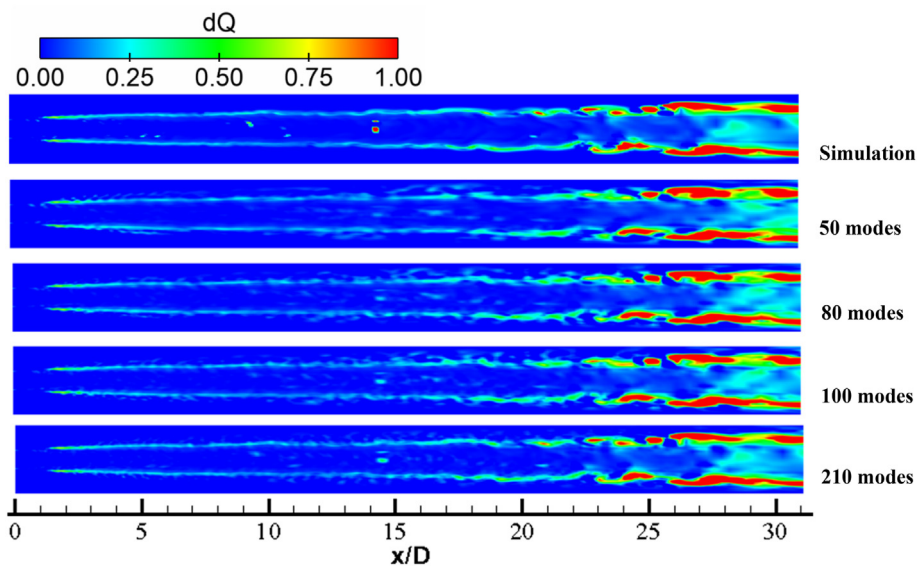

Fig. 12 – Comparison of instantaneous contours of HRR between the original field and POD approximations by retaining different modes.

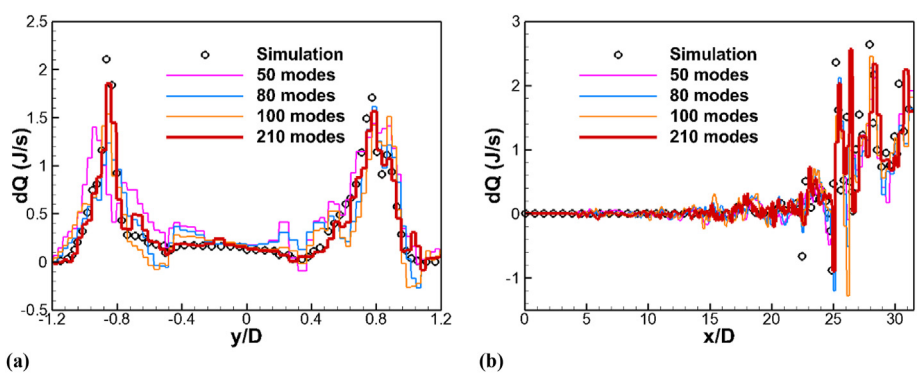

Fig. 13 – Quantitative comparison for the instantaneous HRR between the original field and POD approximations by retaining different modes, (a) x = 30.4D, (b) y = 0.79D.

more POD modes. Fig. 13 quantitatively compares the radial and streamwise profiles for HRR between the original flow field and the POD approximations. The locations of peaks and inflection points are well captured by all the approximations. However, the 50-mode approximation underpredicts the peaks. Additionally, all the approximations exhibit fluctuations except for the 210-mode approximation, which precisely matches the original flow field. Therefore, in the following analysis, 210 POD modes are used for the reconstruction of HRR, and 300 POD modes are used for OH to retain 99% source information. In the ANN training, the first 300 modal coefficients of OH are combined as the input vector,

Table 2 – The best ANN structures for each segmentation.

Segmentation	Modes	Neurons	Epochs	TrainingSetMSE	ValidationSetMSE
1	1–21	(50,50,50)	200,000	9.961e-06	5.730e-03
2	22–41	(50,50,50)	200,000	1.823e-05	6.945e-03
3	42–61	(50,50,50)	200,000	2.478e-05	8.658e-03
4	62–81	(50,50,50)	200,000	3.378e-05	1.086e-02
5	82–101	(50,50,50)	200,000	4.135e-05	1.114e-02
6	102–121	(50,50,50)	200,000	5.451e-05	1.493e-02
7	122–141	(50,50,50)	200,000	5.609e-05	1.441e-02
8	142–161	(50,50,50)	200,000	6.673e-05	1.542e-02
9	162–181	(50,50,50)	200,000	7.733e-05	1.786e-02
10	182–210	(50,50,50)	200,000	7.781e-05	1.795e-02

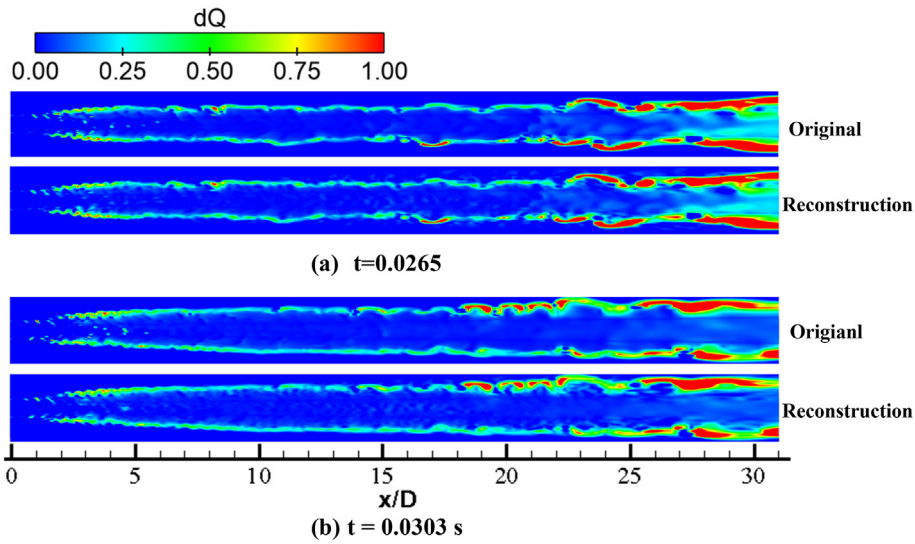

Fig. 14 – The comparison of the instantaneous contours of HRR between the original one and the reconstruction at (a) t = 0.0265 s, (b) t = 0.0303 s.

and the first 210 modal coefficients of HRR constitute the output vector.

Results of segmentation training

To improve the efficiency in the ANN training, the 210-neuron output vector for HRR is segmented into ten subsets, i.e., the new neuron number in each segmented output vector is 21. The 300-neuron input vector for OH is kept the same for each segmented output vector. Another critical aspect of the development of ANN models is the number of neurons in each hidden layer. Increasing the neuron numbers can improve the capacity of the ANN model but will certainly increase the training time. How to determine a proper neuron number in each hidden layer is still an open question for diffident problems. By trial and error, it is found that 50 neurons for each hidden layer can maintain high accuracy yet modest training burden for the problem in this study. The early stopping regularization method is adopted to avoid overfitting during the training. When the training epochs reach 200,000, the

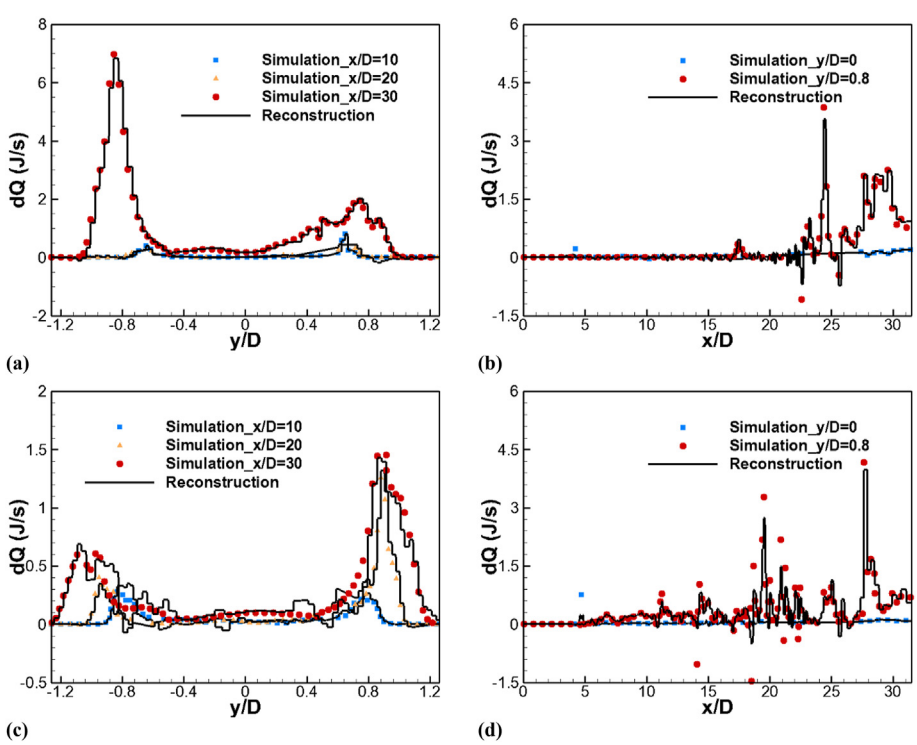

Fig. 15 – The quantitative comparison of the instantaneous HRR between the original one and the reconstruction at (a)–(b) t = 0.00265 s, and (c)–(d) t = 0.00303 s.

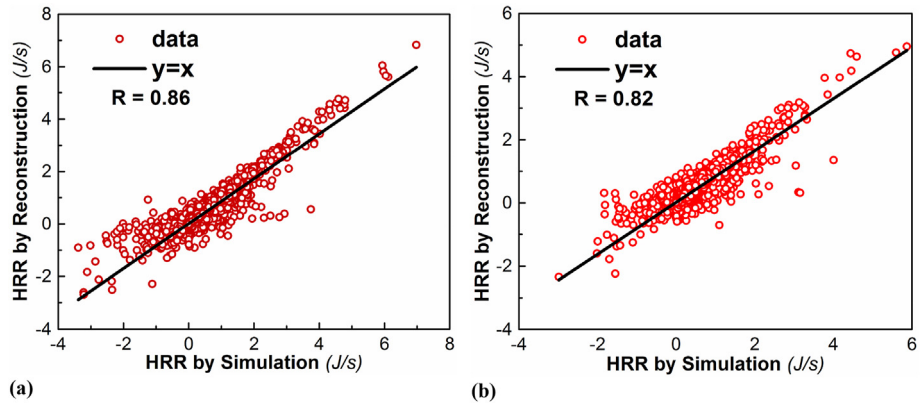

Fig. 16 – Linear regression between the reconstructed and original HRR data at (a) t = 0.0265 s and (b) t = 0.0303 s.

validation set error (ValidationSetMSE) reaches a small value and drops negligibly later; thus, the maximum training epoch is set as 200,000 for each ANN model. The training results for all of the ten subsets are listed in Table 2. The orders of magnitude for TrainingSetMSE and ValidationSetMSE are as small as 10^{-5} and 10^{-2}, respectively.

Performance of the HRR reconstruction framework

To validate the performance of the HRR reconstruction framework, two new data sets are sampled from the modeling at times inside and outside of the 2-FTT sampling window. The training data set is sampled from 0.026 s to 0.03 s with an interval of 1.34×10^{-7} s. The new data sets are sampled at the times of 0.0265 s and 0.0303 s. The first one tests the interpolation capability of the trained ANN model, while the latter test the extrapolation capability.

Using the trained ANN model, the modal coefficients for the two new snapshots are obtained. Then the full fields of dQ are reconstructed based on the derived modal coefficients and the previously-obtained 210 POD modes of HRR. The comparisons of the instantaneous contour for HRR between the original ones and those predicted by the ANN-POD reconstruction model are shown in Fig. 14. No apparent differences are found even for the fine structures in the shear layer. For further demonstration, Fig. 15 conducts the quantitative comparisons at different radial and axial locations, where the agreements are good for both the interpolation and extrapolation cases. The discrepancies at several peaks and trough locations can be further improved by further expanding the input vector to include more POD modes.

The reconstructed HRR versus the original HRR at each cell in the full combustion field is plotted in Fig. 16. The correlation coefficients (R) are 0.86 and 0.82 for the interpolation case at the times of 0.0265 s and the extrapolation case at 0.0303 s, respectively. Since the correlation coefficient above 0.8 is considered highly correlated, the current accuracy of the trained ANN model is satisfactory, which demonstrates the feasibility of reconstructing HRR from OH by using the current proposed ANN-POD model.

In addition, comparing Figs. 4 and 5, it can be seen that prediction can achieve better results for interpolation. It is understandable that the time range of the training data covers the corresponding time points of the interpolation data, while the accuracy of the extension prediction is mainly based on the assumption that the flow situation in each circulation time of the example is consistent, i.e., the flow repeatability. In this case, the data only cover two flow times, not all the transient characteristics of turbulence. Therefore, in order to further improve the accuracy of the extended time point prediction, the training data must include more data in the flow time to ensure sufficient transient turbulence characteristics.

Conclusion

In this study, a novel model based on the reduced-order proper orthogonal decomposition (POD) and the data-driven artificial neural network (ANN) is proposed to reconstruct the spatial distribution of heat release rate (HRR) based on measurable chemiluminescent species OH. The ANN-POD reconstruction model is then validated in a supersonic hydrogen flame, whose instantaneous full-domain HRR distributions at different times are accurately predicted by the trained ANN model and the reduced-order POD models, given the OH distributions.

The main procedures in applying the ANN-POD reconstruction model are as follows, 1) extract POD modes for the HRR and OH snapshots in consecutive time; 2) determine the minimum numbers of POD modes that can precisely approximate the original HRR and OH fields, e.g., m POD modes for OH and n POD modes for HRR; 3) segment the n POD modal coefficients of HRR into l subsets, train individual ANN model for each subset to establish the correlation between the input vector consisting of m modal coefficients of the POD modes of OH, and the output vector consisting of the n/l modal coefficients of the POD modes of HRR; 4) decompose the target OH field to obtain the modal coefficients, derive the modal coefficients of HRR using the trained ANN models, and reconstruct HRR using the derived modal coefficients and the previously-obtained POD modes of HRR.

The application of POD technology effectively reduces the order of the raw flow data in the modeling with 1.728 million cells by a factor of more than 1500 times, which dramatically relieves the computational burden for the ANN models. For

the examined case, the comparison shows that $m = 300$, $n = 210$, and $l = 10$ can provide close approximations to the original flow fields while considerably reducing the ANN training cost. By using the segmentation method, not only the total training time is reduced, but also the accuracy for each individual segmented training can be improved. A simpler ANN structure with three hidden layers and 50 neurons in each hidden layer is used for the segmented training. Interpolation and extrapolation data sets sampled within and outside the time window for the training set are used to validate the ANN-POD reconstruction model. The HRR fields reconstructed from the OH fields agree well with the original HRR fields with correlation coefficients (R) higher than 0.8 for both cases.

This study represents the first attempt to correlate HRR with chemiluminescent species by an ANN model. To generalize the reconstruction framework, a reduced-order POD method was used to extract the most energetic modes from unsteady flows. A novel segmentation method is also developed to reduce the training difficulty and improve training efficiency. The verification in a supersonic hydrogen flame indicates that the reconstruction of HRR from OH is feasible, which is of practical significance for the performance diagnosis and optimization of industrial combustion devices. Once the spatial distribution of HRR can be reconstructed, many technical challenges in combustor design can be reassessed, e.g., 1) optimizing HRR distribution to reduce wall temperature and achieve better thermal management; 2) monitoring HRR distribution in real time to alleviate thermoacoustic coupling oscillation, 3) optimizing the HRR distribution to organize combustion modes and enhance engine thrust. The current HRR prediction method is of great significance for the controlling of combustion modes inside an enclosed combustor and performance-based optimization of engines.

In this study, the OH concentration is obtained from high-fidelity modeling validated by available experimental data. However, in realistic applications, the OH distribution can be obtained via non-intrusive diagnostic techniques, e.g., chemiluminescence, then the real HRR distribution can be obtained by using the proposed ANN-POD reconstruction model. In future work, the current reconstruction model can also be extended to hydrocarbon combustion, for which more chemiluminescent products, e.g., CH and OH, may need to be included to correlate with HRR.

Declaration of competing interest

The authors declare that they have no known competing financial interests or personal relationships that could have appeared to influence the work reported in this paper.

Acknowledgments

The project was supported by National Key Research and Development Program of China (2019YFB1704202), Strategic Priority Research Program of Chinese Academy of Sciences (Grant No. XDA17030X00), and National Natural Science Foundation of China (Grant No. 91641110). The authors are also grateful to the National Supercomputer Center in Tianjin for providing the computational resource.

REFERENCES

[1] Doan NAK, Swaminathan N. Analysis of markers for combustion mode and heat release in MILD combustion using DNS data. Combust Sci Technol 2019;191(5–6):1059–78. https://doi.org/10.1080/00102202.2019.1610746.

[2] Nikolaou ZM, Swaminathan N. Heat release rate markers for premixed combustion. Combust Flame 2014;161(12):3073–84. https://doi.org/10.1016/j.combustflame.2014.05.019.

[3] Touaibi R, Koten H, Boydak O. Parametric study of an organic rankine cycle using different fluids. Int J Sci Emerg Technol 2020;4(2):122–8. https://doi.org/10.28991/esj-2020-01216.

[4] Topçuoğlu K. Trombe wall application with heat storage tank. J Civ Eng 2019;5(7):1477–89. https://doi.org/10.28991/cej-2019-03091346.

[5] Hu Y, Tan J, Lv L, Li X. Investigations on quantitative measurement of heat release rate using chemiluminescence in premixed methane-air flames. Acta Astronaut 2019;164:277–86. https://doi.org/10.1016/j.actaastro.2019.07.019.

[6] Sardeshmukh S, Bedard M, Anderson W. The use of OH* and CH* as heat release markers in combustion dynamics. Int J Spray Combust Dyn 2017;9(4):409–23. https://doi.org/10.1177/1756827717718483.

[7] Fajardo CM, Smith JD, Sick V. PIV, high-speed PLIF and chemiluminescence imaging for near-spark-plug investigations in IC engines. J Phys Conf 2006;45:19–26. https://doi.org/10.1088/1742-6596/45/1/003.

[8] Hardalupas Y, Orain M. Local measurements of the time-dependent heat release rate and equivalence ratio using chemiluminescent emission from a flame. Combust Flame 2004;139(3):188–207. https://doi.org/10.1016/j.combustflame.2004.08.003.

[9] Panoutsos CS, A.M.K.P.Taylor YH. Numerical evaluation of equivalence ratio measurement using OH and CH chemiluminescence in premixed and non-premixed methane-air flames. Combust Flame 2009;156(2):273–91. https://doi.org/10.1016/j.combustflame.2008.11.008.

[10] Hardalupas Y, Panoutsos CS, Taylor AMKP. Spatial resolution of a chemiluminescence sensor for local heat-release rate and equivalence ratio measurements in a model gas turbine combustor. Exp Fluid 2010;49(4):883–909. https://doi.org/10.1007/s00348-010-0915-z.

[11] Kathrotia T, Riedel U, Seipel A, Moshammer K, Brockhinke A. Experimental and numerical study of chemiluminescent species in low-pressure flames. Appl Phys B Laser Opt 2012;107:571–84. https://doi.org/10.1007/s00340-012-5002-0.

[12] Zhang W, Yang X, Wang T, Peng X, Wang X. Experimental study of a gas engine-driven heat pump system for space heating and cooling. J Civ Eng 2019;5(10):2282–95. https://doi.org/10.28991/cej-2019-03091411.

[13] Lauer M, Sattelmayer T. On the adequacy of chemiluminescence as a measure for heat release in turbulent flames with mixture gradients. J Eng Gas Turbines Power 2010;132(6). https://doi.org/10.1115/1.4000126.

[14] Najm HN, Paul PH, Mueller CJ, Wyckoff PS. On the adequacy of certain experimental observables as measurements of flame burning rate. Combust Flame 1998b;113(312).

[15] Najm HN, Knio OM, Paul PH, Wyckoff PS. A study of flame observables in premixed methane - air flames. Combust Sci

Technol 1998;140(1–6):369–403. https://doi.org/10.1080/00102209808915779.
[16] Dirbude SB, Maurya VK. Effect of uniform magnetic field on melting at various Rayleigh numbers. Int J Sci Emerg Technol 2019;3(4):263–73. https://doi.org/10.28991/esj-2019-01189.
[17] Kostikov YA, Romanenkov AM. Approximation of the multidimensional optimal control problem for the heat equation (applicable to computational fluid dynamics (CFD)). J Civ Eng 2020;6(4):743–68. https://doi.org/10.28991/cej-2020-03091506.
[18] Biteau H, Steinhaus T, Schemel C, Simeoni A, Marlair G, Bal N, Torero J. Calculation methods for the heat release rate of materials of unknown composition. Fire Saf Sci 2008;9:1165–76. https://doi.org/10.3801/iafss.fss.9-1165.
[19] Wabel TM, Zhang P, Zhao X, Wang H, Hawkes E, Steinberg AM. Assessment of chemical scalars for heat release rate measurement in highly turbulent premixed combustion including experimental factors. Combust Flame 2018;194:485–506. https://doi.org/10.1016/j.combustflame.2018.04.016.
[20] Ferrarotti M, Amaduzzi R, Bascherini D, Galletti C, Parente A. Heat release rate markers for the adelaide jet in hot coflow flame. Front Mech Eng 2020;6. https://doi.org/10.3389/fmech.2020.00005.
[21] Tinaut FV, Reyes M, Giménez B, Pastor JV. Measurements of OH* and CH* chemiluminescence in premixed flames in a constant volume combustion bomb under autoignition conditions. Energy Fuels 2011;25(1):119–29. https://doi.org/10.1021/ef1013456.
[22] Kocabaş F, Ünal S, Ünal B. A neural network approach for prediction of critical submergence of an intake in still water and open channel flow for permeable and impermeable bottom. Comput Fluids 2008;37(8):1040–6. https://doi.org/10.1016/j.compfluid.2007.11.002.
[23] Goodfellow I, Bengio Y, Courville A. Deep learning. MIT Press; 2016.
[24] Owoyele O, Kundu P, Ameen MM, Echekki T, Som S. Application of deep artificial neural networks to multi-dimensional flamelet libraries and spray flames. Int J Engine Res 2019;21(1):151–68. https://doi.org/10.1177/1468087419837770.
[25] Lapeyre CJ, Misdariis A, Cazard N, Veynante D, Poinsot T. Training convolutional neural networks to estimate turbulent sub-grid scale reaction rates. Combust Flame 2019;203:255–64. https://doi.org/10.1016/j.combustflame.2019.02.019.
[26] Ihme M, Schmitt C, Pitsch H. Optimal artificial neural networks and tabulation methods for chemistry representation in LES of a bluff-body swirl-stabilized flame. Proc Combust Inst 2009;32(1):1527–35. https://doi.org/10.1016/j.proci.2008.06.100.
[27] Ihme M. Construction of optimal artificial neural network architectures for application to chemical systems_comparison of generalized pattern search method and evolutionary algorithm. Artificial Neural Network Appl 2011;7:125–50.
[28] Ling J, Kurzawski A, Templeton J. Reynolds averaged turbulence modelling using deep neural networks with embedded invariance. J Fluid Mech 2016;807:155–66. https://doi.org/10.1017/jfm.2016.615.
[29] Maulik R, San O. A neural network approach for the blind deconvolution of turbulent flows. J Fluid Mech 2017;831:151–81. https://doi.org/10.1017/jfm.2017.637.
[30] Dissanayake M, P.-T N. Neural-network-based approximations for solving partial differential equations. Commun Numer Methods Eng 1994;10:195–201.
[31] Gonzalez RL. Neural networks for variational problems in engineering. PhD thesis. 2008.
[32] Lagaris IE, L A, Fotiadis DI. Artificial neural networks for solving ordinary and partial differential equations. IEEE Trans Neural Network Learn Syst 1998;9(987–1000).
[33] Jambunathan K, Ashforth-Frost S HS, Fontama V. Evaluating convective heat transfer coefficients using neural networks. Int J Heat Mass Tran 1996;39:2329–32.
[34] Milano M, Koumoutsakos P. Neural network modeling for near wall turbulent flow. J Comput Phys 2002;182(1):1–26. https://doi.org/10.1006/jcph.2002.7146.
[35] Faller WE, S S. Neural networks: applications and opportunities in aeronautics,". Prog Aero Sci 1996;32:433–56.
[36] Sen B, Menon S. Representation of chemical kinetics by artificial neural networks for large eddy simulations. In: AIAA/ASME/SAE/ASEE joint propulsion conference & exhibit/43rd; 2007. https://doi.org/10.2514/6.2007-5635.
[37] Azizi S, Ahmadloo E. Prediction of heat transfer coefficient during condensation of R134a in inclined tubes using artificial neural network. Appl Therm Eng 2016;106:203–10. https://doi.org/10.1016/j.applthermaleng.2016.05.189.
[38] Hempert F, Boblest S, Ertl T, Sadlo F, Offenhäuser P, Glass CW, Hoffmann M, Beck A, Munz CD, Iben U. Simulation of real gas effects in supersonic methane jets using a tabulated equation of state with a discontinuous Galerkin spectral element method. Comput Fluids 2017;145:167–79. https://doi.org/10.1016/j.compfluid.2016.12.024.
[39] Zhou Z, He G, Wang S, Jin G. Subgrid-scale model for large-eddy simulation of isotropic turbulent flows using an artificial neural network. Comput Fluids 2019;195:104319. https://doi.org/10.1016/j.compfluid.2019.104319.
[40] Li X, Fan E, Yao W, Fan X. Numerical investigation of characteristic frequency excited highly underexpanded jets. Aero Sci Technol 2017;63:304–16. https://doi.org/10.1016/j.ast.2017.01.005.
[41] Wang J-X, Wu J-L, Xiao H. Physics-informed machine learning approach for reconstructing Reynolds stress modeling discrepancies based on DNS data. Phys Rev Fluids 2017;2(3). https://doi.org/10.1103/PhysRevFluids.2.034603.
[42] Singh AP, Medida S, Duraisamy K. Machine-Learning-Augmented predictive modeling of turbulent separated flows over airfoils. AIAA J 2017;55(7):2215–27. https://doi.org/10.2514/1.j055595.
[43] Maulik R, San O, Rasheed A, Vedula P. Subgrid modelling for two-dimensional turbulence using neural networks. J Fluid Mech 2018;858:122–44. https://doi.org/10.1017/jfm.2018.770.
[44] Shadram Z, Nguyen TM, Sideris A, Sirignano WA. Neural network closure models for estimating flame variables in a liquid-propellant rocket engine. 2019. https://doi.org/10.2514/6.2019-2008.
[45] Bhalla S, Yao M, Hickey JP, Crowley M. Compact representation of a multi-dimensional combustion manifold using deep neural networks. Eur Conf Mach Learn 2019;36:602–17. https://doi.org/10.1007/978-3-030-46133-1_36.
[46] Volkwein S. Proper orthogonal decomposition: theory and reduced-order modelling. Master;s thesis. 2013.
[47] Zhang Y, Zhou L, Meng H, Teng H. Reconstructing cellular surface of gaseous detonation based on artificial neural network and proper orthogonal decomposition. Combust Flame 2020;212:156–64. https://doi.org/10.1016/j.combustflame.2019.10.031.
[48] Oberleithner K. On turbulent swirling jets: vortex breakdown, coherent structures, and their control. Technical University of Berlin; 2012. PHD.
[49] Powell A. Observations of the oscillation modes of choked circular jets. J Acoust Soc Am 1992;92(5):2823–36. https://doi.org/10.1121/1.404398.
[50] Berkooz G, Holmes P, Lumley JL. The proper orthogonal decomposition in the analysis of turbulent flows. Annu Rev

Fluid Mech 1993;25:539–75. https://doi.org/10.1146/annurev.fl.25.010193.002543.
[51] Mak S, Sung C-L, Wang X, Yeh S-T, Chang Y-H, Joseph VR, Yang V, Wu CFJ. An efficient surrogate model for emulation and physics extraction of large eddy simulations. J Am Stat Assoc 2018;113(524):1443–56. https://doi.org/10.1080/01621459.2017.1409123.
[52] Dolci V, Arina R. Proper orthogonal decomposition as surrogate model for aerodynamic optimization. Int J Aero Eng 2016;2016:1–15. https://doi.org/10.1155/2016/8092824.
[53] Fahlaoui T, De Vuyst F. Nonintrusive data-based learning of a switched control heating system using POD, DMD and ANN. Compt Rendus Mec 2019;347(11):793–805. https://doi.org/10.1016/j.crme.2019.11.005.
[54] Yu J, Hesthaven JS. Flowfield reconstruction method using artificial neural network. AIAA J 2019;57(2):482–98. https://doi.org/10.2514/1.j057108.
[55] Lucia DJ, Beran PS, Silva WA. Reduced-order modeling: new approaches for computational physics. Prog Aero Sci 2004;40(1–2):51–117. https://doi.org/10.1016/j.paerosci.2003.12.001.
[56] Lui HFS, Wolf WR. Construction of reduced-order models for fluid flows using deep feedforward neural networks. J Fluid Mech 2019;872:963–94. https://doi.org/10.1017/jfm.2019.358.
[57] Fiala T, Sattelmayer Thomas. Heat release and OH* radiation in laminar non-premixed hydrogen-oxygen flames. In: 51st AIAA aerospace sciences meeting including the new horizons forum and aerospace exposition; 07-10 January, 2013. https://doi.org/10.2514/6.2013-1170.
[58] Fiala T, Sattelmayer T. Heat release and UV–Vis radiation in non-premixed hydrogen–oxygen flames. Exp Fluid 2015;56(7). https://doi.org/10.1007/s00348-015-2013-8.
[59] He L, Guo Q, Gong Y, Wang F, Yu G. Investigation of OH* chemiluminescence and heat release in laminar methane–oxygen co-flow diffusion flames. Combust Flame 2019;201:12–22. https://doi.org/10.1016/j.combustflame.2018.12.009.
[60] Li B, Lee Y, Yao W, Lu Y, Fan X. Development and application of ANN model for property prediction of supercritical kerosene. Comput Fluids 2020;209:104665. https://doi.org/10.1016/j.compfluid.2020.104665.
[61] Rumerlhart David E, H GE, W RJ. Learning representations by back-propagating errors. Nature 1986;323:533–6. https://doi.org/10.1038/323533a0.
[62] Mizutani Eiji, D SE, N K. On derivation of MLP backpropagation from the Kelley-Bryson optimal-control gradient formula and its application,". Proc IEEE Int Joint Conf Neural Network 2000;2:167–72. https://doi.org/10.1109/IJCNN.2000.857892.
[63] Li Y, Fu Y, Li H, Zhang S-W. The improved training algorithm of back propagation neural network with self-adaptive learning rate. In: 2009 international conference on computational intelligence and natural computing; 2009. p. 73–6. https://doi.org/10.1109/cinc.2009.111.
[64] Fiesler E. Neural networks with adaptive learning rate and momentum terms. IDIAP Tech Rep 1995;95–04.
[65] Sirovich L. Turbulence and the dynamics of coherent structures. III. Dynamics and scaling. Q Appl Math 1987;45(3):583–90. https://doi.org/10.1090/qam/910464.
[66] Rodriguez J, S L. Coherent structures and chaos: a model problem. Phys Lett 1987;120(211).
[67] Evans. Application of a Two-dimensional parabolic computer program to prediction of turbulent reacting flows. NASA Tech Pap 1978;3:20–463. 1978STIN...7820463E.
[68] Kee RJ, Rupley FM, Miller JA. Chemkin-II: a fortran chemical kinetics package for the analysis of gas-phase chemical kinetics. Sandia Natl Lab 1996;2. https://doi.org/10.2172/481621. Sandia.
[69] Chase MW. NIST-JANAF Thermochemical Tables. J Phy Chem Ref Data Monogr 1998;2:2–30.
[70] Kee RJ, Dixon-lewis G, Warnatz J, Coltrin ME, Miller JA. A fortran computer code package for the evaluation of gas-phase, multicomponent transport properties. In: Sandia national laboratories. Livermore: California; 1986.
[71] Bird RB, Stewart WE, Lightfoot EN. Viscosity and the mechanisms of momentum transport. In: Transport phenomena (2nd edition). New York: John Wiley & Sons; 2002. p. 27.
[72] Yao W, Lu Y, Wu K, Wang J, Fan X. Modeling analysis of an actively-cooled scramjet combustor under different kerosene/air ratios. J Propul Power 2018;34(4):975–91. https://doi.org/10.2514/1.B36866.
[73] Weller HG, Tabor G, Jasak H, Fureby C. A tensorial approach to CFD using object oriented techniques. Comput Phys 1997;12(6):620–31. https://doi.org/10.1063/1.168744.
[74] Yao W, Lu Y, Li X, Wang J, Fan X. Improved Delayed Detached Eddy Simulation of a high-Ma regenerative-cooled scramjet combustor based on skeletal kerosene mechanism. 2016. https://doi.org/10.2514/6.2016-4761.
[75] Yao W, Wang J, Lu Y, Li X, Fan X. Full-scale Detached Eddy Simulation of kerosene fueled scramjet combustor based on skeletal mechanism. In: 20th AIAA international space planes and hypersonic systems and technologies conference. 2015–3579. Glasgow: Scotland; 2015. AIAA.
[76] Li X, Yao W, Fan X. Large-Eddy simulation of time evolution and instability of highly underexpanded sonic jets. AIAA J 2016;54(10):3191–211. https://doi.org/10.2514/1.j054689.
[77] Li X, Zhou R, Yao W, Fan X. Flow characteristic of highly underexpanded jets from various nozzle geometries. Appl Therm Eng 2017;125:240–53. https://doi.org/10.1016/j.applthermaleng.2017.07.002.
[78] Won-Wook K, Suresh M. A new dynamic one-equation subgrid-scale model for large eddy simulations. In: 33rd aerospace Sciences meeting and exhibit, 95–0356. Reno, NV: American Institute of Aeronautics and Astronautics; 1995. AlAA.
[79] Kim S-E. Large eddy simulation using an unstrcutured mesh based finite-volume solver. In: 34th AIAA fluid dynamics conference and exhibit, 2004–2548. Portland: Oregon; 2004. AIAA.
[80] Kim W-W, Menon S, Kim W-W, Menon S. Application of the localized dynamic subgrid-scale model to turbulent wall-bounded flows. 1997. https://doi.org/10.2514/6.1997-210.
[81] Burke MP, Chaos M, Ju Y, Dryer FL, Klippenstein SJ. Comprehensive H2/O2 kinetic model for high-pressure combustion. Int J Chem Kinet 2012;44(7):444–74. https://doi.org/10.1002/kin.20603.
[82] Li J, Zhao Z, Kazakov A, Dryer FL. An updated comprehensive kinetic model of hydrogen combustion. Int J Chem Kinet 2004;36(10):566–75. https://doi.org/10.1002/kin.20026.
[83] Mobus H, G P, Bruggemann D. Scalar and joint scalar-velocity-frequency Monte Carlo PDF simulation of supersonic combustion. Combust Flame 2003;132.
[84] Yao W, Wu K, Fan X. Influences of domain symmetry on supersonic combustion modeling. J Propul Power 2019;35(2):451–65. https://doi.org/10.2514/1.B37227.